Nonlinear magnetohydrodynamical effects in precessional fishbone oscillations

A. Ödblom, B. N. Breizman, S. E. Sharapov, T. C. Hender, and V. P. Pastukhov

Related Articles

Temporal and spectral evolution of runaway electron bursts in TEXTOR disruptions
Phys. Plasmas 19, 092513 (2012)

Modification of Δ′ by magnetic feedback and kinetic effects
Phys. Plasmas 19, 092510 (2012)

Magneto-modulational instability in Kappa distributed plasmas with self-generated magnetic fields
Phys. Plasmas 19, 092114 (2012)

Multi-dimensional instability of dust-acoustic solitary waves in a magnetized plasma with opposite polarity dust
Phys. Plasmas 19, 093707 (2012)

Nonlinear electron-magnetohydrodynamic simulations of three dimensional current shear instability
Phys. Plasmas 19, 092305 (2012)
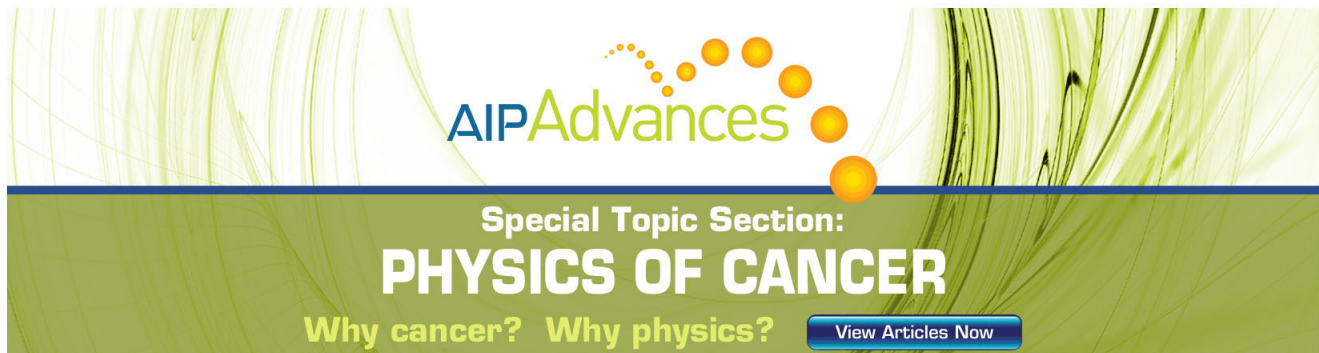
Additional information on Phys. Plasmas

Nonlinear magnetohydrodynamical effects in precessional fishbone oscillations

A. Ödblom
EURATOM/UKAEA Fusion Association, Culham Science Centre, Abingdon, Oxfordshire OX14 3DB, United Kingdom

B. N. Breizman
Institute for Fusion Studies, University of Texas at Austin, Austin, Texas 78712

S. E. Sharapov and T. C. Hender
EURATOM/UKAEA Fusion Association, Culham Science Centre, Abingdon, Oxfordshire OX14 3DB, United Kingdom

V. P. Pastukhov
Institute of Nuclear Fusion, RRC "Kurchatov Institute," 123182 Moscow, Russia

The role of magnetohydrodynamic nonlinearities in precessional $m=n=1$ fishbone oscillations has been analyzed analytically and numerically. The work is based on the reduced magnetohydrodynamic (MHD) equations including a linear energetic particle drive model. When the energetic particle pressure is close to the instability threshold, the top-hat linear eigenmode profile of the ideal MHD $m=1$ radial displacement splits up into a two-step structure around the $q=1$ flux surface, due to the finite frequency ω of the mode. The width of the individual steps is a factor γ/ω smaller than the distance between them, where γ is the growth rate of the mode. We find that the MHD nonlinearities modify the mode structure further, and produce explosive nonlinear growth, accompanied by frequency chirping, for modes that are near the instability threshold. The results are quite different for fishbone oscillations that are excited well above the stability threshold. The growth rates of these linearly fast growing modes decreases nonlinearly and the MHD nonlinearities are stabilizing in this limit. The nonlinear MHD effects are important when the plasma displacement is comparable to, or larger than, the scale length of the fishbone structure. © 2002 American Institute of Physics. [DOI: 10.1063/1.1421373]

I. INTRODUCTION

An oscillatory "fishbone" instability, with toroidal mode number $n=1$ and poloidal mode number $m=1$, was first observed in experiments with perpendicular neutral beam injection (NBI) on the Poloidal Divertor Experiment (PDX) tokamak.[1] The instability occurs in repetitive bursts, with the mode frequency decreasing by about a factor of 2 during each burst. Large fishbone bursts are observed to cause losses of NBI-produced energetic ions, thus reducing the efficiency of plasma heating. Experimentally, the radial plasma displacement in the fishbone mode was found to be similar to the "top-hat" structure of the internal $n=1$ kink mode[2,3] associated with the safety factor $q=1$ in tokamak plasmas. The frequency of the fishbone oscillations in PDX was found to be close to the magnetic precession frequency of the trapped energetic ions, $\langle\omega_{dh}\rangle = -i\langle\mathbf{V}_{dh}\cdot\boldsymbol{\nabla}\rangle$, as well as to the thermal ion diamagnetic frequency, ω_{*pi}. Here $\mathbf{V}_{dh}$ is the guiding center toroidal precession velocity, and the notation $\langle\ldots\rangle$ represents averaging over the bounce time of the energetic ion orbit. The first theoretical interpretation[4] of the fishbones established the resonant wave particle interaction at the magnetic precession frequency of energetic ions, $\omega = \langle\omega_{dh}\rangle$, as a key drive of this instability.

Two different regimes have been identified for the linear phase of fishbone instability.[4,5] The first regime of so-called "precessional" fishbones[4] refers to the case when the mode frequency ω in the plasma reference frame is much greater than the thermal ion diamagnetic frequency ω_{*pi},

$$\omega \gg \omega_{*pi}. \tag{1}$$

In this case, trapped energetic ions destabilize the $n=1, m=1$ mode when the mode frequency ω resonates with the frequency of their precessional motion $\langle\omega_{dh}\rangle$. The mode frequency emerges from the Alfvén continuum, so the mode structure has singularities at the radial locations, r_A, where the conditions of local Alfvén resonance,

$$\omega = \pm k_{\|m}(r_A)V_A(r_A), \tag{2}$$

are fulfilled for a given fishbone frequency ω; here $V_A(r)$ is the Alfvén velocity, and $k_{\|m}$ the wave vector parallel to the equilibrium magnetic field $\mathbf{B}_0$, $k_{\|m}(r) \equiv (i/B_0)(\mathbf{B}_0\cdot\boldsymbol{\nabla})$. Due to the continuum damping associated with the fluid resonances, Eq. (2), the precessional fishbones, Eq. (1), are excited at relatively high values of the energetic (hot) ion beta, $\beta_{\text{hot}} \equiv 4\pi P_{\text{hot}}/\mathbf{B}_0^2 > \beta_{\text{hot}}^{\text{crit}}$. Here P_{hot} is the pressure of energetic ions and the threshold $\beta_{\text{hot}}^{\text{crit}}$ is determined by the

155

balance[4] between the fishbone kinetic drive due to the energetic ions, γ_{hot}, and the fishbone Alfvén continuum damping, γ_{MHD}:

$$\gamma_{\text{hot}}(\beta_{\text{hot}}^{\text{crit}}) = \gamma_{\text{MHD}}. \tag{3}$$

The second linear regime refers to the fishbones with[5] $\omega \approx \omega_{*pi}$. In this case, the structure of the Alfvén continuum is strongly affected by the branch of $\omega = \omega_{*pi}$ oscillations, and a low-frequency "gap" is formed in the Alfvén continuum. The $\omega \approx \omega_{*pi}$ fishbone mode lies within this frequency "gap" so that condition (2) is not fulfilled and under these conditions the Alfvén continuum damping is negligible for the $\omega \approx \omega_{*pi}$ fishbone.

Fishbone oscillations were later observed in many other tokamaks with significant populations of energetic ions produced by ion cyclotron resonance heating (ICRH), perpendicular and parallel NBI (see Ref. 6 and references therein). A more complete linear theory of fishbones emerged that accounts for the transit resonances of the energetic ions[7] and finite orbit width corrections of the energetic ion drive.[8,9]

The characteristic burstlike structure of the fishbone oscillations and the significant decrease of the oscillation frequency of the mode within a single burst indicate that during their evolution fishbones have a strongly nonlinear character.[6] Empirical predator-prey type models (see, e.g., Appendix C of Ref. 10) as well as a more complete model[11] were developed to interpret the repetitive bursts of the $\omega \approx \omega_{*pi}$ fishbones and the accompanying losses of energetic ions as a result of a redistribution of energetic ions due to the perturbation field of fishbones. The models[10,11] based on the kinetic wave particle trapping nonlinearity retain the essential physics of the $\omega \approx \omega_{*pi}$ fishbones, since the kinetic nonlinearity appears to be the dominant one when the fishbones are in the diamagnetic ω_{*pi} gap. The gap essentially eliminates the fluid resonance, $\gamma_{\text{MHD}} = 0$. This regime allows a perturbative description of the mode, which makes the problem technically similar to the bump-on-tail problem, as well as to many other wave-particle interaction problems (see Ref. 11 and references therein).

A nonlinear description of the precessional fishbones ($\omega \gg \omega_{*pi}$) presents a more challenging problem: an interplay of kinetic and fluid resonances during the fishbone evolution. One can see from Eq. (3) that the linear responses from the kinetic and fluid resonances are almost equal near the instability threshold. However, their nonlinear responses are very different and a special investigation is needed in order to assess the importance of the fluid nonlinearity, in addition to the kinetic nonlinearity similar to that analyzed in Ref. 11.

In this paper, we concentrate on the role of the fluid nonlinearity in the precessional fishbones, regime (1). In order to delineate the effects of the fluid nonlinearity we consider a fishbone evolution, during which the energetic ion response remains linear at all times and the effects of the kinetic nonlinearity can be neglected.

The nonlinear MHD model for the fishbones is presented in Sec. II of this paper. Fishbone modes are strongly extended along the equilibrium magnetic field, $k_\parallel \ll k_\perp$, so that the fast magnetosonic degrees of freedom, $\omega \cong k_\perp V_A$, are

essentially not excited during the instability and the fishbone oscillations are of the Alfvénic type. It is important to note that the fluid nonlinearity, which is known[12] to be small for local Alfvén waves satisfying the dispersion relation $\omega = k_\parallel V_A$, is not small for the global fishbone mode satisfying Eq. (2) at two radial positions, $r = r_A$, only. In order to focus on the fluid nonlinearity, which is relevant for the Alfvénic type global mode, and to exclude the magnetosonic oscillations, we use the nonlinear reduced MHD model[13,14] combined with a linear response for the energetic particles.

Analysis of the reduced MHD model for fishbones is performed analytically in Sec. III. It is shown that near the instability threshold, $\gamma_{\text{hot}} - |\gamma_{\text{MHD}}| \ll \gamma_{\text{hot}}$, the radial structure of the fishbone mode of frequency ω has two singular layers, one inside and one outside the $q = 1$ surface. The radial locations, r_A, of the resonance layers are determined in accordance with Eq. (2) by

$$\omega^2 = (1 - q(r_A))^2 (V_A(r_A)/Rq(r_A))^2. \tag{4}$$

R is the major radius of the magnetic axis. Near the instability threshold of the fishbone, the radial width of each singular layer is smaller by a factor γ/ω than the distance between the layers, where $\gamma(\ll \omega)$ is the instability growth rate, $\gamma \equiv \gamma_{\text{hot}} - |\gamma_{\text{MHD}}|$. Under these conditions, the fluid nonlinearity becomes important when the plasma displacement is comparable to the width of each singular layer near the $q = 1$ surface, whereas the particle nonlinearity can still be negligible at this level. It is shown in Sec. III that the dominant effects of the fluid nonlinearity in fishbones are caused by a generation of a $m = 0$ poloidal plasma flow, and a $m = 0$ poloidal magnetic field. The generation of the $m = 0$ magnetic field, $\tilde{B}_p^{(0)}$, can be considered as a flattening of the "effective" safety factor profile $q(r, t) = rB_T/R(B_p + \tilde{B}_p^{(0)})$. The toroidal and poloidal magnetic equilibrium fields are denoted with B_T and B_p, respectively.

It is found that the early stage of the near-threshold fishbone instability, during which the two resonant layers, Eq. (4), are well separated, is characterized by an explosive behavior of the mode amplitude, accompanied by a fast change in the mode frequency. The mode evolution when the two resonant layers coalesce and a possible scenario for the mode saturation (similar to Ref. 3), or a decelerated growth of the mode, are discussed.

In order to investigate the nonlinear MHD effects in the fishbone regime beyond the explosive phase a numerical reduced MHD model is used in Sec. IV. The model applies to a cylindrical geometry. The energetic particle drive is added to the model in the form of a prescribed term, which is obtained in terms of moments of the energetic ion distribution function in toroidal geometry. This drive remains linear during the fishbone evolution. A direct benchmarking of the numerical model with the analytically predicted linear and explosive regimes of the fishbone instability is performed. The effect of the mode saturation due to MHD nonlinearity is investigated for strongly driven fishbones in the regime where γ/ω is large. Conclusions are presented in Sec. V.

II. REDUCED MHD MODEL

We start from the MHD equation of motion

$$\rho\left(\frac{\partial \mathbf{V}}{\partial t}+\mathbf{V}\cdot\nabla\mathbf{V}\right)=-\nabla p_c-\nabla\cdot\overset{\leftrightarrow}{\mathbf{P}}_{\text{hot}}+\frac{1}{c}\mathbf{j}\times\mathbf{B}, \tag{5}$$

where ρ, $\mathbf{V}$ and p_c are the mass density, velocity, and pressure of the core plasma, $\mathbf{j}$ and $\mathbf{B}$ are the plasma current and magnetic field, and $\overset{\leftrightarrow}{\mathbf{P}}_{\text{hot}}\equiv P_{\perp h}\mathbf{I}-(P_{\perp h}-P_{\parallel h})\mathbf{bb}$ is the tensor of hot ion anisotropic pressure that drives the fishbone instability. Here I is the unit tensor, $\mathbf{b}=\mathbf{B}/B$, and $P_{\perp h}$ and $P_{\parallel h}$ are the perpendicular and parallel components of the hot ion pressure which must be obtained in terms of moments of the energetic ion distribution function. In addition to Eq. (5), the frozen-in equation for the core plasma is used,

$$\frac{\partial \mathbf{B}}{\partial t}=\nabla\times[\mathbf{V}\times\mathbf{B}], \tag{6}$$

together with the Maxwell's equations

$$\nabla\times\mathbf{B}=\frac{4\pi}{c}\mathbf{j}, \tag{7}$$

$$\nabla\cdot\mathbf{B}=0. \tag{8}$$

The fishbone mode is extended along the equilibrium magnetic field $\mathbf{B}_0$, so that a small parameter relates the longitudinal (along $\mathbf{B}_0$) and the perpendicular (with respect to $\mathbf{B}_0$) scales of the mode: $\nabla_\parallel\cong\varepsilon\nabla_\perp$, where $\varepsilon=r/R\cong B_p/B_T\ll1$ is the inverse aspect ratio of the tokamak. Considering plasmas with typical beta values $\beta\cong\varepsilon^2$, one can disregard both the linear and the nonlinear coupling of the shear Alfvén wave characterizing the fishbone oscillation and the fast magnetosonic waves. For the Alfvénic type of perturbations we follow the reduced MHD ansatz[13,14] and introduce two stream functions, $\dot u$ and α, to represent the components of the perturbed plasma velocity and magnetic field perpendicular to the vacuum magnetic field $\mathbf{B}_T$:

$$\mathbf{V}=\nabla\dot u\times\mathbf{B}_T, \tag{9}$$

$$\mathbf{B}=\mathbf{B}_T+\nabla\alpha\times\mathbf{B}_T. \tag{10}$$

Here and below the dot denotes $\partial/\partial t$. Representing the plasma velocity in terms of the stream function in Eq. (9) implies that we are considering an incompressible plasma flow,

$$\nabla\cdot\mathbf{V}=0. \tag{11}$$

The vorticity equation is derived from the charge conservation equation for a quasi-neutral plasma, $\nabla\cdot\mathbf{j}=0$, which can be manipulated nonlinearly to explicitly extract the curvature $\boldsymbol{\kappa}_T=\mathbf{b}_T\cdot\nabla\mathbf{b}_T$ of the *vacuum* magnetic field lines, $\mathbf{B}_T=\mathbf{b}_T B_T$. Using Eqs. (7) and (8) gives a differential equation in a form similar to the one given in Ref. 15, namely

$$B_T\mathbf{B}\cdot\nabla j_\parallel-B_T\mathbf{B}\cdot\nabla\times(\mathbf{j}\times\mathbf{B})+2B_T\mathbf{B}\times\boldsymbol{\kappa}_T\cdot(\mathbf{j}\times\mathbf{B})$$

$$=j_\parallel(\mathbf{B}_T\cdot\nabla B_T+B_T\mathbf{B}_\Delta\cdot\boldsymbol{\kappa}_T)-(j_\parallel\mathbf{b}_T\cdot\nabla\ln B_T+2\mathbf{j}\cdot\boldsymbol{\kappa}_T)\mathbf{B}_T$$

$$\cdot\mathbf{B}_\Delta+\mathbf{j}\cdot\nabla(\mathbf{B}_T\cdot\mathbf{B}_\Delta), \tag{12}$$

where $j_\parallel=\mathbf{b}_T\cdot\mathbf{j}$ and $\mathbf{B}_\Delta=\mathbf{B}-\mathbf{B}_T$. We insert the $\mathbf{j}\times\mathbf{B}$-force from Eq. (5) in Eq. (12), and apply the reduced MHD representations (9), (10) for which $\mathbf{B}_T\cdot\mathbf{B}_\Delta=0=\mathbf{B}_T\cdot\mathbf{V}$. Furthermore, we neglect the weak gradients of the plasma density, $\rho=\rho_0=$ constant, and omit effects of p_c. The final vorticity equation can be then written as

$$\Delta_\perp\ddot u=-(\mathbf{V}\cdot\nabla)\Delta_\perp\dot u+\frac{1}{4\pi\rho_0}(\mathbf{B}\cdot\nabla)\Delta_\perp\alpha$$

$$-\frac{1}{\rho_0}[\mathbf{b}_T\times(\mathbf{b}_T\cdot\nabla)\mathbf{b}_T]\cdot\nabla\frac{P_{\perp h}}{B_T}. \tag{13}$$

Substituting Eqs. (9), (10) in Eq. (6) we obtain the flux equation

$$\dot\alpha=(\mathbf{B}\cdot\nabla)\dot u. \tag{14}$$

The reduced MHD equations (13), (14) with an additional term representing the pressure of trapped hot ions, $P_{\perp h}$, which drives the fishbone instability, are the basis for the analysis of nonlinear MHD effects in the fishbone mode.

We consider an equilibrium with monotonic $q(r)$-profile and $q(0)<1$. The energetic ion pressure profile is localized close to the plasma center, well inside the $q=1$ surface, so that there are no energetic ions in the vicinity of the $q=1$ surface. We also suppose that no equilibrium flow exists in the plasma at $t=0$, i.e., $\mathbf{V}_0=0$.

In order to analyze Eqs. (13), (14), we decompose α and u into Fourier series

$$(\alpha,u)=\exp[in\zeta-i\omega_0 t]\sum_m\ (\alpha(r,\tau),u(r,\tau))$$

$$\times\exp[-im\theta]+\text{c.c.}, \tag{15}$$

where ζ, θ and r are the toroidal, poloidal and radial coordinates such that $\hat r\cdot\hat\theta\times\hat\zeta=1$. A two-scale time dependence, which is relevant to nonlinear fishbone evolution near the threshold, is taken into account here, $\partial/\partial\tau\ll\omega_0$, where ω_0 is the fishbone frequency. For further simplicity, we neglect during the linear stage of fishbone instability, the toroidal coupling between poloidal harmonics, which is important for the ideally unstable $n=1$ kink mode.[2] The perturbed stream functions describing the fishbone mode are then only associated with the mode numbers $n=m=1$, so for the linear stage of fishbone we take

$$(u,\alpha)=(u_1,\alpha_1)e^{i\zeta-i\theta-i\omega_0 t}+\text{c.c.} \tag{16}$$

In the near-threshold case, the difference between large drive and large damping is relatively small, $\gamma_{\text{hot}}-|\gamma_{\text{MHD}}|\ll\gamma_{\text{hot}}\approx|\gamma_{\text{MHD}}|$. This small difference corresponds to the net linear growth rate γ of the mode. In order to assess the role of nonlinear MHD effects analytically, we consider the limit of a weak MHD nonlinearity, in which the nonlinear parts of Eqs. (13), (14) just begin to compete with the small linear "net" term corresponding to the difference between large drive and large damping. An iteration procedure can be applied in this limit of weak nonlinearity, with the linear relation

$$\alpha_1 = i \frac{B_T}{R} \left(1 - \frac{1}{q} \right) u_1, \tag{17}$$

used as the first iteration. The relation Eq. (17) is obtained from Eq. (14) by using the expression

$$(\mathbf{B} \cdot \nabla) = \frac{B_T}{R} \frac{\partial}{\partial \zeta} + \frac{B_P}{r} \frac{\partial}{\partial \theta} = i \frac{B_T}{R} \left(1 - \frac{1}{q} \right). \tag{18}$$

In order to incorporate nonlinear effects we consider u and α as a sum of the main harmonic Eq. (16) and two satellite harmonics

$$u = u_0 + (u_1 e^{i\zeta - i\theta - i\omega_0 t} + u_2 e^{2[i\zeta - i\theta - i\omega_0 t]} + \text{c.c.}), \tag{19}$$

$$\alpha = \alpha_0 + \tilde{\alpha}_0 + (\alpha_1 e^{i\zeta - i\theta - i\omega_0 t} + \alpha_2 e^{2[i\zeta - i\theta - i\omega_0 t]} + \text{c.c.}), \tag{20}$$

where α_0, $\tilde{\alpha}_0$ are the components of the stream functions representing the equilibrium poloidal magnetic field, and the nonlinearly generated poloidal magnetic field, respectively. Substituting Eqs. (19)–(20) into Eq. (14) we obtain expressions for the nonlinearly generated zeroth and second harmonics of the poloidal field stream function,

$$\tilde{\alpha}_0 = \frac{B_T^2}{Rr} \frac{\partial}{\partial r} \left[\left(1 - \frac{1}{q} \right) u_1 u_{-1} \right], \tag{21}$$

$$\alpha_2 = 2i \frac{B_T}{R} \left(1 - \frac{1}{q} \right) u_2 - \frac{B_T^2}{2rR} \frac{q'}{q^2} u_1^2, \tag{22}$$

where prime denotes radial derivative.

We substitute Eq. (19) in Eq. (13) and use the expressions for $\tilde{\alpha}_0$, α_1, and α_2 from Eqs. (17), (21) and (22) in order to consider Eq. (13) in the layer regions, $r \approx r_A$, in which

$$\Delta_\perp = \left(\frac{\partial}{\partial r} \gg \frac{m}{r} \right) \approx \frac{1}{r} \frac{\partial}{\partial r} r \frac{\partial}{\partial r}. \tag{23}$$

The resulting equations show that contributions from the second harmonic are small in comparison with the zeroth harmonic contribution by the ratio of the layer width to the minor radius. By neglecting these small second-harmonic terms, we obtain the following nonlinear MHD equations for the fishbone dynamics in the layer region:

$$\ddot{\psi}_1' + \frac{V_A^2}{R^2} \left(1 - \frac{1}{q} \right)^2 \psi_1' = \rho(t,r) e^{-i\omega_0 t} - 2 \frac{V_A^2}{R^2} \left(1 - \frac{1}{q} \right)^2$$

$$\times \psi_1' (\psi_1 \psi_{-1})'' - 2\omega_0 \psi_1' \dot{\psi}_0', \tag{24}$$

$$\ddot{\psi}_0 = i \left[\omega_0^2 - \frac{V_A^2}{R^2} \left(1 - \frac{1}{q} \right)^2 \right] \cdot (\psi_1 \psi_{-1}' - \psi_{-1} \psi_1'), \tag{25}$$

where $\psi_1 \equiv -B_T(u_1/r)$, $\psi_0 \equiv B_T(\tilde{u}_0/r)$.

The second term in the right-hand side of Eq. (24) arises from the nonlinearly generated $m = 0$ magnetic field, and is of the form $\sim -2V_A R^{-1} (1 - q^{-1}) V_A \tilde{B}_{\theta, m=0} r^{-1} B_T^{-1} \psi_1'$. The third term is due to the $m = 0$ plasma rotation, and is of the form $\sim -2\omega_0 \tilde{V}_{\theta, m=0} r^{-1} \psi_1'$. The first term in the right-hand side of Eq. (24) accounts for the first harmonic of the

perturbed pressure of the hot ions, $\delta P_{\perp h}$, which enters the equation in the form of an integral over radius:

$$\frac{1}{r^3} \int_0^r r^2 \left\{ \frac{1}{\rho_0} [\mathbf{b}_T \times (\mathbf{b}_T \cdot \nabla) \mathbf{b}_T] \cdot \nabla \frac{\delta P_{\perp h}}{B_T} \right\}_1 dr$$

$$= \frac{\rho(t,r)}{B_T} e^{-i\omega_0 t}, \tag{26}$$

where subscript 1 denotes the first component of the Fourier decomposition. The fishbone mode, excited by the toroidal precessional motion of the resonating trapped hot ions, is therefore governed by a volume integral weighted by the profiles of the hot ions and the fishbone mode. As long as the fast particle response is linear, the quantity $\rho(t,r)$ is a linear functional of $\psi_1(-\infty;t)$.

III. ANALYSIS OF FISHBONE EQUATIONS NEAR MARGINAL STABILITY

For the weakly nonlinear regime we make an expansion of ψ_1 in the mode amplitude as $\psi_1 = \psi_1^{(0)} + \psi_1^{(1)} + \dots$, where $\psi_1^{(0)}$ is a linear solution of Eq. (24). As a first step of our analysis we separate linear and nonlinear plasma responses described by Eqs. (24), (25).

A. Linear phase of the fishbone instability

The linear phase of the fishbone evolution is described by the linear limit of Eqs. (24), (25):

$$(\ddot{\psi}_1^{(0)})' + \frac{V_A^2}{R^2} \left(1 - \frac{1}{q} \right)^2 (\psi_1^{(0)})' = \rho(t,r_*) e^{-i\omega_0 t}. \tag{27}$$

The first harmonic only, $n = m = 1$, is involved in the linear phase of the fishbone instability. Away from the resonance layers near $q(r^*) = 1$, the radial structure of the $n = m = 1$ radial displacement,[4] $\xi_1 = i\psi_1^{(0)}$, has a top-hat structure, i.e.,

$$\xi_1(r,t) = \xi_1(r=0,t) = \xi(t), \quad r < r_*$$
$$\xi_1(r,t) = 0, \quad r > r_*. \tag{28}$$

We use Eq. (28) as boundary conditions, $\xi_1(\infty,t) = 0$, $\xi_1(-\infty,t) = \xi(t)$, for the resonance layer equation (27). The solution of Eq. (27), which corresponds to these boundary conditions has for a sufficiently small initial perturbation the following integral form:

$$\psi_1^{(0)} = \int_\infty^x dx_1 \int_0^\infty d\tau \frac{\sin \Omega \tau}{\Omega} \rho(t - \tau, r_*) e^{-i\omega_0(t-\tau)}, \tag{29}$$

where $x \equiv r - r_*$ and

$$\Omega \equiv \frac{V_A}{R} \left(1 - \frac{1}{q} \right). \tag{30}$$

The fast particle response Eq. (26) is averaged over the entire region within the $q = 1$ magnetic surface. Therefore, Eqs. (29) and (30) express the linear solution of the fishbone in terms of the on-axis displacement $\xi(t)$, which determines entirely the perturbed hot ion pressure that drives the instability. In the case of deeply trapped energetic ions, $P_{\parallel h} \ll P_{\perp h}$, Eq. (26) can be reduced to a model relation between $\rho(t,r)$ and $\psi_1^{(0)}(-\infty;t)$ (see Appendix A for details):

$$\rho(t,r)\exp(-i\omega_0 t)\equiv -\frac{\Omega'}{\pi}K\frac{r_*^3}{r^3}\int_{-\infty}^{t}\frac{T\dot{\psi}_1^{(0)}(-\infty;\tau)}{[T-i(\tau-t)]^2}d\tau,$$

(31)

where T is a characteristic precession period for energetic ions, $\Omega'=d\Omega/dr|_{q=1}$, and the dimensionless parameter K is a normalized energetic ion content. The model Eq. (31) for the energetic ion response leads to the linear dispersion relation for precessional fishbones:

$$i=K\int_0^{\infty}\frac{z\exp(-z)}{z-\omega T-i0}dz.$$

(32)

Real and imaginary parts of Eq. (32) determine the threshold value of K for instability and the eigenfrequency ω_0 of the precessional fishbone at the threshold:

$$K_0\cong 0.91,$$

(33)

$$\omega_0\cong 1.35/T.$$

(34)

B. Weakly nonlinear phase of the fishbone instability

Close to marginal stability, $K-K_0\ll K_0$, we substitute the linear solution Eq. (29) into the two nonlinear terms in the right-hand side of Eq. (24) and obtain iteratively the next order solution:

$$(\psi_1^{(1)})'=\int_0^{\infty}d\tau\frac{\sin\Omega\tau}{\Omega}[-2\Omega^2(\psi_1^{(0)})'(\psi_1^{(0)}\psi_{-1}^{(0)})''$$

$$-2\omega_0(\psi_1^{(0)})'\dot{\psi}_0'],$$

(35)

where ψ_0 is determined by Eq. (25) with Eq. (29) substituted in the right-hand side.

At the instability threshold the fishbone has an oscillatory solution, $\psi_1(-\infty;t)\equiv a\exp(-i\omega_0 t)$, where the mode frequency is determined by Eq. (34). Near the instability threshold, a slow time dependence of the mode amplitude has to be accounted for, $a=a(t)$, $|\dot{a}/a|\ll\omega_0$. Following the procedure developed for weakly nonlinear models in Refs. 16–17 we represent $\rho(t,r_*)$ in the following form:

$$\rho=L_1 a+L_2 da/dt,$$

(36)

where L_1 and L_2 determine the frequency and linear growth rate as follows:

$$\omega_0=\operatorname{Im}\bar{L}_1+\gamma_L\operatorname{Im}\bar{L}_2\approx\operatorname{Im}\bar{L}_1,$$

(37)

$$\gamma_L=-\frac{\operatorname{Re}\bar{L}_1}{1+\operatorname{Re}\bar{L}_2}.$$

(38)

Here, $L_j=\Omega'\bar{L}_j/\pi$ $(j=1,2)$ are identified by first Taylor expanding the Fourier transformed Eq. (31) around ω_0, so it is cast into the form of Eq. (36). We introduce a dimensionless time variable, $\bar{t}$, and mode amplitude, $\bar{a}$:

$$\bar{t}\equiv\Gamma t=t(i\omega_0-\pi L_1/\Omega')\cdot(1+\pi L_2/\Omega')^{-1}e^{i\phi},$$

(39)

$$\bar{a}\equiv a\left|\frac{|L_1|^2\Lambda}{2\Gamma^3(i\omega_0-\pi L_1/\Omega')}\right|^{1/2},$$

(40)

where $\Gamma>0$, and ϕ are real constants, and

$$\Lambda=\int_0^{\infty}d\tau_3\frac{1-\exp(2i\omega_0\tau_3)}{\tau_3}$$

has a value of the order of $\ln(\omega_0/\gamma)\gg 1$. In the following text we drop the bar notations. With the use of Eq. (36) we reduce Eq. (35) to the following nonlinear form in the dimensionless variables (see Appendix B):

$$\exp(i\phi)\frac{da}{dt}=a-\frac{|i\omega_0-\pi L_1/\Omega'|}{i\omega_0-\pi L_1/\Omega'}$$

$$\times\int_0^{\infty}d\tau\int_0^{\infty}d\tau_1\int_0^{t-\tau}d\tau_2(\tau+\tau_1)a(t-\tau-\tau_1)$$

$$\times[\dot{a}^*(\tau_2-\tau-\tau_1)a(\tau_2)$$

$$-a^*(\tau_2-\tau-\tau_1)\dot{a}(\tau_2)].$$

(41)

We see then that Eq. (41) admits a self-similar solution that becomes singular during a finite time t_0. For example, we can look for a particular solution of Eq. (41) of the form:

$$a=\frac{R}{(t_0-t)^2}\exp[i\sigma\ln(t_0-t)],$$

(42)

where R and σ are constants. By substituting Eq. (42) in Eq. (41) one obtains the following governing equation for the constants which determine the accelerated (explosive) growth:

$$ie^{i\phi}=R^2\int_0^{\infty}dx\int_0^{x}dz\frac{z\exp\left(i\sigma\ln\left(\frac{(1+x)(1+z)}{1+x+z}\right)\right)}{(1+x)^2(1+z)^2(1+x+z)^2}$$

$$\times\left\{\frac{2+i\sigma}{2-i\sigma}\frac{z+x}{1+z+x}-\frac{z}{1+x}-\frac{x}{1+z}\right\}.$$

(43)

By Taylor expanding the dispersion relation Eq. (32), as well as $L_j(K,\omega_0)$, around the threshold values (ω_0,K_0), we infer $(i\omega_0-\pi L_1/\Omega')/|i\omega_0-\pi L_1/\Omega'|=-i$ as used in Eq. (43), and from the definition of ϕ in Eq. (39) we find $\phi\cong 0.363$. Substituting this value for ϕ in Eq. (43) and computing the integral in right-hand side numerically, we find that Eq. (43) is satisfied for $\sigma\cong-6.5$ (see Appendix C).

Note that while the $(t_0-t)^{-2}$ divergence of solutions of the Eq. (41) is robust, the particular solution Eq. (42) is not unique. Depending on initial conditions, the nonlinear system Eq. (41) may asymptote to other divergent solutions of a more general type than Eq. (42) (see Ref. 18, for example).

It is seen, however, that no saturation due to the MHD nonlinearity exists for the fishbone in the near-threshold case. Such a nonlinear saturation similar to what is given in Ref. 3 should dominate the nonlinear MHD evolution in the case when the two Alfvén resonance layers $r=r_A$ merge and form a single broad layer at the $q=1$ surface. Numerical analysis is required for studying this stage.

IV. NUMERICAL RESULTS

In this section we present numerical simulations relating to the linear and nonlinear evolution of precessional fishbone oscillations. These results will be shown to confirm the ana-

lytical predictions of an explosive growth for fishbone oscillations that are close to the instability threshold. Moreover, we have also explored the nonlinear regime of modes that are well above the marginal stability limit.

For the purpose of these simulations we have cast the reduced MHD equations (9), (10), (13) and (14) in a dimensionless form by normalizing the magnetic fields with the vacuum field, B_T, all length scales with the minor radius, a, and all times with the Alfvén time, $\tau_A = R/V_A$. In order to control the numerical dissipative effects we have also added a resistive (η) as well as a viscous (ν) term so that in terms of the variables $\phi \equiv \tau_A B_T \tilde{u}/a^2$ and $\Psi \equiv -R\alpha/a^2$ the equations are of the form

$$\frac{\partial \Psi}{\partial t} = -R\mathbf{B}\cdot\nabla\phi + \frac{\eta J_\zeta}{S_\eta},$$

$$\frac{\partial U}{\partial t} = -\mathbf{V}\cdot\nabla U - R\mathbf{B}\cdot\nabla J_\zeta + \nu\nabla_\perp^2 U - R^2\mathbf{b}_T\times\boldsymbol{\kappa}_T\cdot\nabla\tilde{P}_{\perp h},$$
$$(44)$$

where $U = \nabla_\perp^2\phi$, $J_\zeta = \nabla_\perp^2\Psi$, $\mathbf{V} = \nabla\phi\times\hat{\zeta}$, $\mathbf{B} = \hat{\zeta} - \nabla\Psi\times\hat{\zeta}/R$. S_η is the magnetic Reynolds number.

The drive of the energetic particles, which are assumed to be confined well inside the $q=1$ magnetic surface, has been included in two alternative ways: either as a boundary condition on an annular simulation layer, or as a source term in the plasma core. In the latter case the dimensionless pressure perturbation ($\tilde{P}_{\perp h}/\rho V_A^2 \to \tilde{P}_{\perp h}$) of the energetic ions is taken in the form

$$\tilde{P}_{\perp h} = Ne^{i\zeta}H(r/r_h)\int_{-\infty}^{t}d\tau\frac{V_{r1}(0,\tau)T}{(T-i(\tau-t))^2} + \text{c.c.}, \quad (45)$$

where H prescribes the radial drive profile and is normalized as $\int_0^a H(r/r_h)r\,dr = r_h^2/2$. Here, N is chosen to match the total drive defined by Eqs. (26) and (31), i.e., $N = 2sKar_*^2/\pi r_h^2 R$. $V_{r1}(0,t)$ is the $m=n=1$ Fourier coefficient of the radial velocity evaluated near the magnetic axis. Linear and nonlinear numerical results in cylindrical geometry based on Eqs. (44) and (45) have been presented in Ref. 19. In a full cylindrical geometry, the nonlinear MHD effects in the fast particle region may compete with the nonlinear MHD effects in the resonant layers, and this makes the interpretation difficult. In the present paper, we will present numerical results that are entirely due to the nonlinear effects in the inertial layer region. It is then sufficient to consider a narrow annular layer, in which no fast particles are present, around the $q=1$ surface. In this case, the energetic ion drive enters the problem through the boundary condition, instead of the energetic term in Eq. (44) that vanishes in the layer. An appropriate boundary condition that is valid well away from the inertial layer so that $\omega^2 \ll \Omega^2$, can be obtained from the linear part of Eq. (24), with Eq. (31) inserted, which gives the integral relation

$$V'_{r1} = -\frac{sKr_*^2}{\pi r^3\Omega^2}\left(\frac{V_{r1}}{T} - i2\int_{-\infty}^{t}d\tau\frac{TV_{r1}}{(T-i(\tau-t))^3}\right). \quad (46)$$

Condition Eq. (46) is valid at the inner boundary where we have neglected the weak variation of the $m=n=1$ profile in the core plasma and taken $V_{r1}(0,\tau) \approx V_{r1}(r,\tau)$ in the right-hand side of Eq. (46). For all other harmonics, which are localized in the inertial region, we impose $\phi=0$ at the inner boundary. The condition at the outer boundary has been taken as $\phi=0$ for $m=1$, and $\phi'=0$ for $m\neq 1$.

For simplicity we have chosen a case with no equilibrium current density in the annular region, and all the current within the center of the annulus. From Ampere's law we infer the current density in the form $j_\zeta = B_T(2-s)/\mu_0 qR$, where s is the magnetic shear, $s \equiv rq'/q$, which we have taken as a constant so that $q = (r/r_*)^s$, with $s=2$. The qualitative features of the fishbone model are not sensitive to the choice of s, which has been confirmed in the numerical simulations with $s=1$, 2, and 3, respectively. Also, the reduced MHD representations (9) and (10) of the cylindrical tokamak, where only the two-dimensional perpendicular motion is important, does not[20] include the drive of the ideal $n=1$ MHD kink mode. Finally, to study the fishbone in its simplest form we diminish the importance of the cylindrical effects by choosing a fairly large radius r_* of the $q=1$ surface, $r_*/a = 0.84$. The computational layer is centered around r_*, i.e., $|r-r_*| \leq \Delta_L$.

Standard numerical techniques have been employed to solve the initial value problem posed by Eqs. (44)–(46) in cylindrical geometry as in Ref. 21, by Fourier expanding in the poloidal and the toroidal angle with finite differences in the radial direction. The numerical solutions have been found to be well converged, and it is noted that the width of the annular layer needs to be chosen wide enough to separate the nonlinear action in the inertial layer from the linear boundary drive in Eq. (46). Performing the computations in an annular layer, rather than in an entire cylinder, gives numerical benefits since it shrinks the computational domain, and reduces the highest frequency Ω in the problem, which in turn reduces the largest value of the global mode profile since $B_r \sim \Omega V_r/\omega$, where $\Omega \gg \omega$ away from the inertial layer. This is essential since the achievable amplitude is for a given time step limited by a numerical instability appearing well away from the inertial region due to the explicit treatment of the nonlinear MHD terms in this integro-differential problem.

We have as an independent consistency check solved the analytically reduced equations (24), (25), and (31) numerically with a finite difference scheme, which gives results that are consistent with the more complete model Eq. (44). It is, however, noted that the numerical results of the analytically reduced equations depend rather sensitively on ω_0, here being a parameter rather than determined by the simulation itself. A 5% mismatch in ω_0 creates an imbalance between the nonlinear terms in Eqs. (24) and (25), so that the MHD nonlinearities act to stabilize rather than destabilize.

For benchmark purposes, it is useful to generalize the reduced model equations (24) and (25) to arbitrary amplitude by keeping the nonlinear terms in a closed form, rather than truncating its nonlinear expansion. With the $m=0$ and $m=1$ harmonics included we note that Eq. (14) can for $m=1$ be written in the dimensional form

$$\dot{\alpha}_1 + \widetilde{\mathbf{V}}_0 \cdot \nabla \alpha_1 = (\mathbf{B}_0 + \widetilde{\mathbf{B}}_0) \cdot \nabla \dot{u}_1 \equiv i \frac{B_T}{V_A} \Omega_{\mathrm{NL}} \dot{u}_1, \qquad (47)$$

where

$$\Omega_{\mathrm{NL}} \equiv \Omega - \frac{V_A \widetilde{B}_{\theta, m=0}}{r B_T}. \qquad (48)$$

Inserting Eq. (47) in Eq. (14) gives for $m=0$ the generalization of Eq. (21) to the closed form result as

$$\dot{\bar{\alpha}}_0 = \frac{V_A}{r} \frac{\partial}{\partial r} \left(\frac{1}{\Omega_{\mathrm{NL}}} \frac{\partial}{\partial t} (\alpha_1 \alpha_{-1}) \right). \qquad (49)$$

With Eq. (47) inserted into

$$\dot{V}_{\theta, m=0} = \left(V_r B_T \nabla_\perp^2 \dot{u} - \frac{B_r}{4\pi\rho_0} B_T \nabla_\perp^2 \alpha \right)_{m=0}, \qquad (50)$$

we find with use of Eq. (23) the generalized version of the reduced Eq. (25) in the form

$$\ddot{\psi}_0 = i \left(\omega^2 - \frac{\Omega_{\mathrm{NL}}^2}{(1 + \widetilde{V}_{\theta, m=0}/r\omega)^2} \right) \cdot (\psi_1 \psi'_{-1} - \psi_{-1} \psi'_1). \qquad (51)$$

Equation (24) can be generalized in an analogous way. Equations (49) and (51) simplify to Eqs. (21) and (25) in the limit $\widetilde{V}_{\theta, m=0}/r \sim \widetilde{B}_{\theta, m=0}/r\sqrt{4\pi\rho_0} \ll \omega$. Equations (49)–(51) have been used to benchmark the code for $\nu=0$, and a perfect agreement was obtained for the generation of the $m=0$ magnetic field. The frequency needed to evaluate Eqs. (50) and (51) is inferred from the local rotation of the mode structure in the poloidal cross section. Good agreement for the $m=0$ poloidal velocity profile is obtained when the radial profile of the local growth rate, as inferred from the numerical solution, is included in the comparison.

A. Linear results

1. Threshold and mode frequency of the fishbone instability

The numerical results for the *linear* growth rate γ and frequency ω of the fishbone model are summarized in Figs. 1–2. From Fig. 1, where we have used $T/\tau_A = 40$, $\Delta_L/a = 0.10$ and $\eta = 0 = \nu$, we infer that the fishbone mode is excited in the numerical simulation when the normalized fast particle content K exceeds the predicted analytical threshold value $K_0 \cong 0.91$ given in Eq. (33), implying good agreement between numerical and analytical threshold physics for the fast particle drive as well as the Alfvén continuum damping.

The fishbone frequency varies only weakly with the fast particle content as shown in Fig. 1, and agrees fairly well with the analytical prediction Eq. (34) as inferred from the linear dispersion relation Eq. (32). The slight frequency offset ($\omega/\omega_0 = 0.93$) is a consequence of the finite radial width of the computational domain, since the (weak) variation in the central plasma of the $m=1$ radial displacement profile is ignored numerically, whereas it is accounted for in the analytical treatment. To quantify the width dependence in the numerical dispersion relation we found for the slowest growing case in Fig. 1, a reduction in frequency to $\omega/\omega_0 = 0.86$
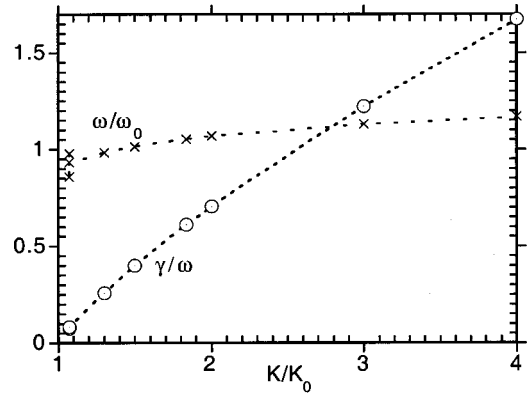

FIG. 1. Linear numerical results for γ/ω and ω/ω_0 as a function of the normalized fast particle content K/K_0, where γ and ω denote the growth rate and frequency, respectively, and K_0 and ω_0 are the analytical threshold values in Eqs. (33) and (34).

when the layer width was halved, and an increase to $\omega/\omega_0 = 0.98$ when the width was doubled. At the same time the ratio γ/ω was almost unchanged.

The precessional dependence of the mode frequency $\omega \sim T^{-1}$, where T is the characteristic toroidal precession period of the energetic particles as introduced in Eq. (31), is well preserved numerically as shown in Fig. 2.

2. Double layer structure in the linear eigenmode profile

When the energetic particle pressure, $\beta_{\mathrm{hot}} B^2/4\pi$, slightly exceeds the threshold value $\beta_{\mathrm{hot}}^{\mathrm{crit}} \sim s r \omega/V_A$, the top-hat linear eigenmode profile splits up into a two-step structure in the inertial region around the $q=1$ surface due to the finite frequency ω of the mode. Steep gradients appear in the radial eigenmode profile where the magnetic field line bending is balanced by the inertial terms, $\omega = \pm \Omega$. The radial splitting distance is $\Delta \sim r R \omega/s V_A$, whereas the inner width δ of each layer is a factor γ/ω smaller. The numerical solution is in quantitative agreement with the linear analytical eigenmode profile inferred from Eq. (27) as illustrated in Fig. 3 where $\gamma/\omega \cong 8\%$, $\eta = 0 = \nu$, $T/\tau_A = 40$.
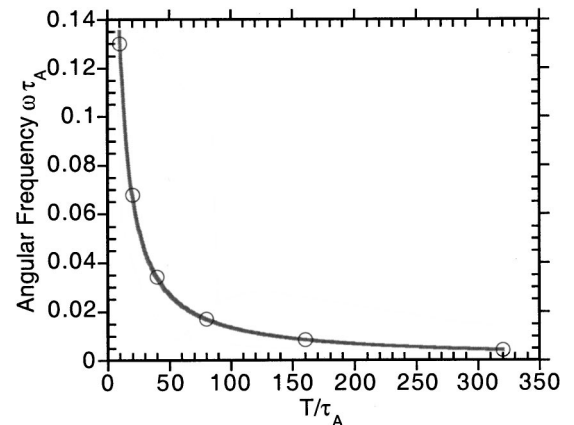

FIG. 2. Linear angular frequency ω versus the toroidal precessional time T for $K/K_0 = 1.5$ in the numerical simulations (circle), and from the analytical solution (34), $\omega = 1.35/T$ (solid).
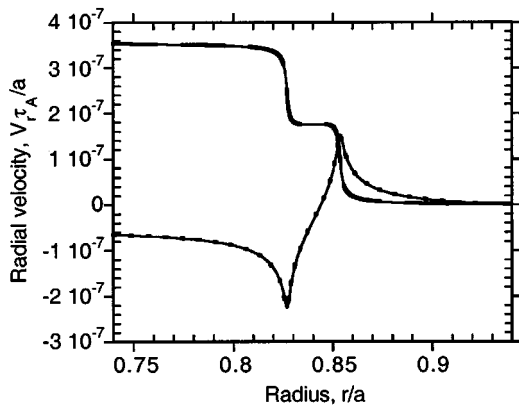
FIG. 3. The real and imaginary part of the $n=m=1$ Fourier component of the linear radial velocity profile for a mode near the instability threshold, $\gamma/\omega \cong 8\%$. Analytical profiles are shown as thick dashed curves, and are reproduced in the numerical simulation (thin solid curves) for $\eta=0=\nu$, $T/\tau_A=40$.

FIG. 5. The nonlinear growth rate evolution of the $m=1$ radial velocity amplitude, $\gamma=\partial \ln|V_r|/\partial t$, for a mode near the instability threshold, $\gamma/\omega \sim 8\%$, and its dependence on the numerical spectral resolution: $m=0-8$ (thick solid), $m=0-4$ (short dashed), $m=0-2$ (long dashed), $m=0-1$ (solid with markers). Here, $T/\tau_A=40$.

B. Nonlinear results

1. Modes near the instability threshold

The most striking nonlinear result of the numerical simulations is the demonstration of a destabilizing or, depending on the parameter regime, a stabilizing influence of the MHD nonlinearities in the inertial layer, combined with a rapid and significant frequency chirping. For modes slightly above the instability threshold, the numerical results confirm the analytical prediction in Sec. III B of an accelerated nonlinear growth as illustrated in Fig. 4 where $\gamma/\omega \sim 8\%$. Shown in Fig. 4, which is the nonlinear evolution of the layer simulation in Fig. 3 where $T/\tau_A=40$, $\eta=0=\nu$, and $m=0-8$, is the time evolution of the real and imaginary parts of the velocity potential, in comparison with the analytical explosive growth rate prediction as well as with a linear growth. The mode amplitude exceeds significantly the indicated linear values, $|\phi| \sim \exp(\gamma_L t)$, in the later part of the simulation when the nonlinear terms become important. Moreover, the numerical evolution of the amplitude agrees quantitatively with the analytical explosive prediction equation (42), where $|\phi| \sim 1/(t_0-t)^p$ with the exponent $p=2$, for $\omega_0 t_0/2\pi$
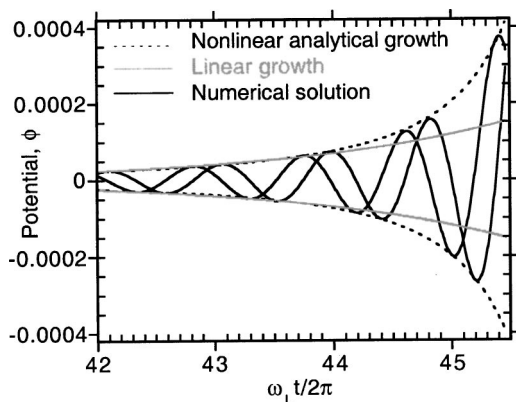

FIG. 4. The $m=1$ amplitude evolution in the numerical solution (solid black), and as predicted by the explosive analytical envelope (dashed), in contrast to a linear growth (solid gray), for a mode near the instability threshold, $\gamma/\omega \sim 8\%$, with $m=0-8$, $\eta=0=\nu$, $T/\tau_A=40$.
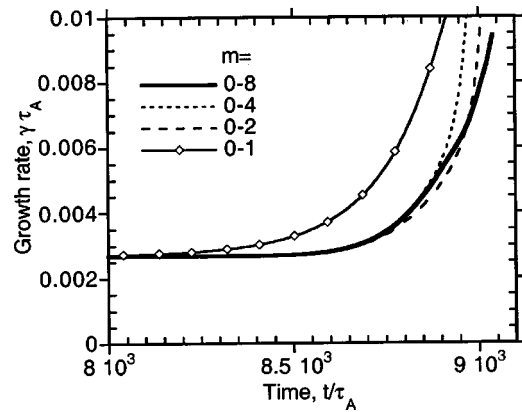
$=46.56$. The rapid nonlinear acceleration of the fishbone instability in Fig. 4 gives an order unity change in the growth rate within a single oscillation as shown in Fig. 5.

The sensitivity of the numerical results to the spectral resolution is examined in Fig. 5, where the number of poloidal and toroidal Fourier harmonics in this single helicity problem, $m/n=1$, is increased from 2 to 9 with $m \geq 0$, for the same parameters as in Fig. 4. One of the most robust features of the solution is the accelerated $m=1$ growth in the nonlinear regime, which is well captured with only two harmonics included in the computation, namely $m=0$ and $m=1$. At least the qualitative evolution of the weakly nonlinear evolution is therefore well described by only the $m=n=0$ and the $m=n=1$ Fourier harmonics, a fact that was used in the analytical analysis in Sec. III B. However, the quantitative onset of the nonlinear increase in the growth rate is delayed to start at a larger $m=1$ amplitude, when several harmonics are retained, for the case considered in Fig. 5.

The nonlinear effects are expected to become important when the kink displacement is of the order of the scale length of the mode structure, i.e., when $\xi_r \sim \delta$. Since $\delta=\gamma/\Omega'$ with $\Omega'\tau_A=s/rq$ we find for the case considered in Fig. 4, where $\gamma\tau_A \approx 2.7 \times 10^{-3}$, the magnetic shear $s=2$, and $q=1$ at $r/a=0.84$, that $\delta/a \sim 1.1 \times 10^{-3}$. From Fig. 4 we infer that the nonlinear evolution starts when the dimensionless $\phi \sim 6 \times 10^{-5}$ at $r/a=0.74$ which corresponds to the displacement $\xi_r/a \sim \phi/r\omega \sim 2.6 \times 10^{-3}$, in qualitative agreement with the simple estimate.

The mode profiles evolve nonlinearly, not only by an increase in the amplitude as in the linear regime, but by a change in shape as well. In particular, the steep individual steps in the two-step structure of the linear eigenmode profile in Fig. 3 are broadened nonlinearly due to the accelerated growth rate, and the layers start to merge when γ/ω approaches unity. Since numerical issues limit the complete exploration of the merging phase, we have instead studied the nonlinear evolution of modes that in the linear regime start with $\gamma/\omega > 1$. Results for these linearly fast growing modes are given in the section below.

Phys. Plasmas, Vol. 9, No. 1, January 2002

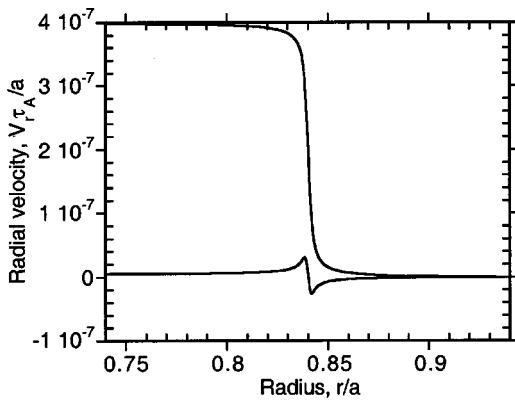Nonlinear magnetohydrodynamic effects . . .   163

FIG. 6. The real and imaginary parts of $m=n=1$ Fourier coefficient for the linear radial velocity profile when $\gamma/\omega \sim 2$. Here, $\nu\tau_A/a^2 = 10^{-9}$, $T/\tau_A = 1280$.

FIG. 7. The functional dependence of γ/ω, where $2\gamma = d \ln E_1/dt$ is inferred from the $m=n=1$ energy E_1 in the layer, on the amplitude of the $m=n=1$ radial velocity, $|V_{r1}|$, for a mode well above the instability threshold, $\gamma_L/\omega_L \sim 2$, and its convergence with increasing spectral resolution: $m = n = 0-12$ (solid thick), $0-8$ (thin solid), $0-4$ (short dashed), $0-2$ (long dashed), $0-1$ (solid with markers).

2. Modes well above the instability threshold

Up to now we have presented results for linearly slowly growing modes that are near the instability threshold. These modes are *destabilized* by the MHD nonlinearities. For example, the ratio γ/ω increases nonlinearly in Fig. 5 for the slightly unstable mode from $\gamma/\omega \sim 8\%$ to 20% (where a numerical instability limited further progress). The situation is quite different for modes that are fast growing ($\gamma/\omega \gg c_{\mathrm{crit}} \sim 1$) in the linear regime; a case which is somewhat similar to the $n=1$ ideal MHD kink instability characterized by a single layer. Nonlinear MHD effects for the ideal $n=1$ kink were considered in Ref. 3. We might expect to observe a similar behavior in our case even though the drive is of different origin. In this case the fluid nonlinearities are *stabilizing* and their effect is similar to the one discussed in Ref. 3. To see this we consider the nonlinear evolution of a fast growing mode with $\gamma/\omega \sim 2$. In this case, the two separated layers of the linear eigenmode profile in Fig. 3 coalesce, and appear as a single layer, as exemplified in Fig. 6 where we used $T/\tau_A = 1280$, $\eta = 0$, and $\nu\tau_A/a^2 = 10^{-9}$. If the energetic particle drive is well above the instability threshold value, $(K-K_0)/K_0 \sim 1$, the rapid linear growth of the mode is reduced in the nonlinear regime as illustrated in Fig. 7, where γ/ω drops from 2 in the linear regime to a value of the order of 0.5, and the growth rate is approximately halved. It is worth noting that as in the case of slowly growing modes it suffices to include only the $m=0$ and $m=1$ Fourier harmonics to capture the nonlinearly stabilizing effect. However, the onset amplitude for nonlinear behavior is again increased when more harmonics are included, as shown in Fig. 7.

V. SUMMARY AND DISCUSSION

The role of magnetohydrodynamic nonlinearities in precessional $m=n=1$ fishbone oscillations has been analyzed analytically and numerically. The work is based on the reduced MHD equations in a cylindrical tokamak, including a linear energetic particle drive model. When the energetic particle pressure is close to the instability threshold, the top-hat linear eigenmode profile of the ideal MHD $m=1$ mode splits up into a two-step structure around the $q=1$ flux surface, due to the finite frequency ω of the mode. The width of the
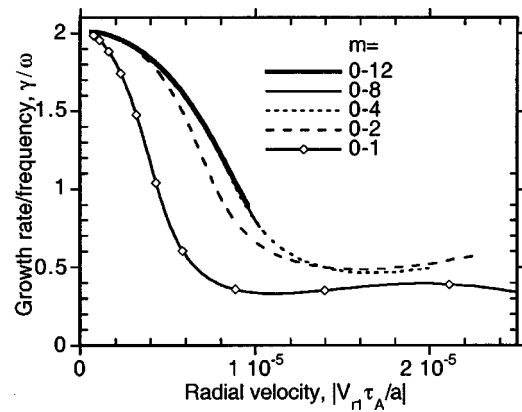
individual steps is a factor γ/ω smaller, where γ is the growth rate of the mode. The numerical solutions of the reduced MHD equations are in quantitative agreement with the analytical linear eigenmode profile. Also, the simulations agree with the analytical predictions for the mode frequency and the growth rate near the instability threshold. Thus, we have a good understanding of the linear properties of the precessional fishbone oscillations.

The key finding in the nonlinear regime, for modes near the instability threshold, is that the nonlinear MHD terms produce an explosive growth. The mode structure in the inertial layer changes during the explosive phase, and is accompanied by frequency chirping. We have a good understanding for the explosive growth of the mode amplitude, whereas a more complete understanding of what determines the changes in the phase, i.e., the chirping rate, requires further work, which is in progress. However, the self-consistent changes in the mode structure during the nonlinear evolution are already accounted for in the analytical as well as numerical analysis. An interesting feature of the model is the nonlinear generation of a $m=0$ poloidal flow, as well as a $m=0$ poloidal magnetic field. Here, it is noted that it is still an open question whether the drive of these $m=0$ fields remains efficient in toroidal tokamak geometry.

We have found that fishbone oscillations that grow slowly, with respect to the mode frequency, in the linear regime are thus destabilized nonlinearly. A reduced nonlinear equation was derived, and its analytical solution was compared with the numerical results. The analytically predicted explosive growth, $|\phi| \sim 1/(t_0-t)^p$ with the exponent $p=2$, is well reproduced in the numerical simulations. These nonlinear effects become important when the radial plasma displacement is of the order of the radial scale length of the two-step structure. The nonlinear results are quite different for fishbone oscillations that are excited well above the stability threshold. The growth rate of these linearly fast growing modes decreases nonlinearly, and the MHD nonlinearities are stabilizing in this limit; a similar result was found for

the nonlinear saturation of the internal kink mode.[3]

Thus, we have a good understanding of the linear features of the precessional fishbone oscillations, as well as the nonlinear explosive evolution of the mode amplitude for modes that are excited near the instability threshold.

ACKNOWLEDGMENTS

APPENDIX A: MODEL FOR LINEAR RESPONSE OF DEEPLY TRAPPED HOT IONS

In order to describe the motion of the energetic ions, we use the guiding center Lagrangian derived by Littlejohn[22] and adopted to a large-aspect-ratio tokamak with circular flux surfaces in Ref. 23

$$L = P_\zeta \dot{\zeta} + P_\theta \dot{\theta} + P_\gamma \dot{\gamma} - H_0(P_\zeta; P_\theta; P_\gamma) - V. \quad (A1)$$

Here the angle variables for the unperturbed motion are the toroidal angle ζ, the poloidal angle θ, and the gyro angle γ. The actions conjugate to the corresponding angles are

$$P_\zeta = -\frac{eB_0}{c}\int_0^r \frac{r' \, dr'}{q(r')} + MR_0 u_\parallel, \quad (A2)$$

$$P_\theta = \frac{e}{2c} B_0 r^2, \quad (A3)$$

$$P_\gamma = \frac{Mc}{e}\mu, \quad (A4)$$

where e is the charge of the ion, M the ion mass, $\mu = MV_\perp^2/(2B)$, $u_\parallel$ and $V_\perp$ are components of the ion velocity along the equilibrium magnetic field and perpendicular to the equilibrium magnetic field. H_0 is the Hamiltonian of the unperturbed motion,

$$H_0 = \mu B_0 \left(1 - \frac{r}{R_0}\cos\theta\right) + \frac{1}{2}Mu_\parallel^2, \quad (A5)$$

and

$$V = \frac{e}{c}B_0 r \left\{\frac{\partial \psi}{\partial t} + u_\parallel(\mathbf{b}_0 \cdot \nabla)\psi\right\}, \quad (A6)$$

is the part due to the interaction between the ion and plasma perturbation associated with the $m = n = 1$ mode.[24]

In the simplified case of deeply trapped energetic ions the terms with $u_\parallel$ in Eqs. (A2), (A5), and (A6) are negligibly small. Also, for these ions $\theta \to 0$. The bounce motion of the trapped ions is then degenerated and the particle motion can be described by the toroidal precession only. In this essentially one-dimensional limit the bounce averaged linearized kinetic equation for the hot ion distribution function δf is simplified to

$$\frac{\partial}{\partial t}\delta f + \Omega_\zeta \frac{\partial}{\partial \zeta}\delta f - \left\{iV_0 e^{-i\omega_0 t + i\zeta}\frac{\partial F_h}{\partial P_\zeta} + \text{c.c.}\right\} = 0, \quad (A7)$$

where $F_h(\mu; E; P_\zeta)$ is the equilibrium distribution function of the hot ions. Here

$$\Omega_\zeta \equiv \frac{\partial H_0}{\partial P_\zeta} \quad (A8)$$

is the toroidal precession frequency, and the Fourier decomposed interaction part of the Lagrangian,

$$V \equiv \sum_l \ (V_l e^{-i\omega t + i\zeta - il\theta} + \text{c.c.}), \quad (A9)$$

has the following dominant component due to the $m = n = 1$ mode:

$$V_0 e^{-i\omega t} \approx r\dot{\psi}_1 \frac{eB_0}{c}. \quad (A10)$$

The solution of the simplified kinetic equation (A7) has the following form:

$$\delta f = i\frac{\partial F_h}{\partial P_\zeta} e^{i\zeta}\int_{-\infty}^t e^{i\Omega_\zeta(\tau - t)} r\frac{eB_0}{c}\dot{\psi}_1 d\tau + \text{c.c.}, \quad (A11)$$

so that the perturbed anisotropic pressure,

$$\delta P_{\perp h} = \int \mu B_0 \cdot \delta f \cdot d^3\mathbf{V}, \quad (A12)$$

leads to the driving term Eq. (26) in the form

$$\rho e^{-i\omega_0 t} \approx \frac{iV_A^2}{\pi r^3 B_0 R_0^2}\int d^3 x \, d^3 V \mu \delta f e^{-i\zeta}. \quad (A13)$$

APPENDIX B: ANALYSIS OF THE WEAKLY NONLINEAR SOLUTION EQUATION (35)

With the use of Eq. (29), the nonlinear terms in the right-hand side of Eq. (35) take the form

$$\psi_1^{(0)}\psi_{-1}^{(0)} = \int_\infty^x dx_2 \int_\infty^x dx_3 \int_0^\infty d\tau_2 \int_0^\infty d\tau_3$$
$$\times \frac{\sin \Omega_2 \tau_2}{\Omega_2}\frac{\sin \Omega_3 \tau_3}{\Omega_3}\rho(t - \tau - \tau_2)$$
$$\times \rho^*(t - \tau - \tau_3)e^{i\omega_0(\tau_2 - \tau_3)}, \quad (B1)$$

and

$$\dot{\psi}_0(x; t - \tau) = i\int_0^{t-\tau} d\tau_4 \int_0^\infty d\tau_2 \int_0^\infty d\tau_3 [\omega_0^2 - \Omega^2]$$
$$\times \rho(\tau_4 - \tau_2)\rho^*(\tau_4 - \tau_3)e^{i\omega_0(\tau_2 - \tau_3)}$$
$$\times \left[\int_\infty^x d\tilde{x}\frac{\sin \tilde{\Omega}\tau_2}{\tilde{\Omega}}\frac{\sin \Omega \tau_3}{\Omega}\right.$$
$$\left. - \int_\infty^x d\tilde{x}\frac{\sin \tilde{\Omega}\tau_3}{\tilde{\Omega}}\frac{\sin \Omega \tau_2}{\Omega}\right]. \quad (B2)$$

The solution of Eq. (35) due to the nonlinear driving force in the RHS is then represented in the form

$$\psi_1(+\infty) - \psi_1(-\infty) = -\psi_1(-\infty) = A + B, \qquad \text{(B3)}$$

where the nonlinear terms, A and B, are obtained from Eqs. (B1) and (B2) as follows:

$$A = -2\int_0^\infty d\tau \int_0^\infty d\tau_1 \int_0^\infty d\tau_2 \int_0^\infty d\tau_3 \rho(t-\tau-\tau_1)\rho(t-\tau-\tau_2)$$

$$\times \rho^*(t-\tau-\tau_3)e^{-i\omega_0(t-\tau-\tau_1-\tau_2+\tau_3)}$$

$$\times \int_{-\infty}^{+\infty} dx\, \Omega^2 \frac{\sin\Omega\tau}{\Omega}\frac{\sin\Omega\tau_1}{\Omega}\frac{\partial^2}{\partial x^2}$$

$$\times \left(\int_\infty^x dx_2 \frac{\sin\Omega_2\tau_2}{\Omega_2}\int_\infty^x dx_3 \frac{\sin\Omega_3\tau_3}{\Omega_3} \right), \qquad \text{(B4)}$$

$$B = -2i\omega_0 \int_0^\infty d\tau \int_0^\infty d\tau_1 \int_0^\infty d\tau_2 \int_0^\infty d\tau_3 \int_0^{t-\tau} d\tau_4 \cdot \rho(t-\tau-\tau_1)\rho(\tau_4-\tau_2)\rho^*(\tau_4-\tau_3)e^{-i\omega_0(t-\tau-\tau_1-\tau_2+\tau_3)}$$

$$\times \left\{ \int_{-\infty}^{+\infty} dx\, \frac{\sin\Omega\tau \sin\Omega\tau_1}{\Omega}\frac{\partial}{\partial x}\left(\left(\omega_0^2 + \frac{\partial^2}{\partial\tau_3^2} \right)\int_\infty^x d\tilde{x}\, \frac{\sin\tilde\Omega\tau_2}{\tilde\Omega}\frac{\sin\Omega\tau_3}{\Omega} - \left(\omega_0^2 + \frac{\partial^2}{\partial\tau_2^2} \right)\int_\infty^x d\tilde{x}\, \frac{\sin\tilde\Omega\tau_3}{\tilde\Omega}\frac{\sin\Omega\tau_2}{\Omega} \right) \right\}. \qquad \text{(B5)}$$

We make a substitution $\tau_2 \leftrightarrow \tau_3$ wherever necessary and integrate over τ_2. The relation

$$\delta(t_0,t) = \frac{1}{\pi}\int_0^\infty d\Omega\, \cos\Omega(t_0-t) \qquad \text{(B6)}$$

is used to simplify the integration. The resulting expression can be integrated over x by introducing $\Omega' = d\Omega/dx$, so that $dx = d\Omega/\Omega'$ to give

$$A \approx -\frac{\pi e^{-i\omega_0 t}}{2\omega_0^2 \Omega'}\int_0^\infty d\tau \int_0^\infty d\tau_1 \int_0^\infty d\tau_3 \frac{\tau+\tau_1}{\tau_3}\rho(t-\tau-\tau_1)$$

$$\times [\rho(t-\tau-\tau_3)\rho^*(t-2\tau-\tau_1-\tau_3)$$

$$- e^{2i\omega_0\tau_3}\rho(t-\tau-\tau_3)\rho^*(t-2\tau-\tau_1+\tau_3)], \qquad \text{(B7)}$$

$$B \approx \frac{\pi e^{-i\omega_0 t}}{\omega_0^2 \Omega'}\int_0^\infty d\tau \int_0^\infty d\tau_1 \int_0^\infty d\tau_3 \int_0^{t-\tau} d\tau_4 \frac{\tau+\tau_1}{\tau_3}$$

$$\times (1-e^{2i\omega_0\tau_3})\rho(t-\tau-\tau_1)\rho(\tau_4-\tau_3)\dot\rho^*(\tau_4-\tau-\tau_1). \qquad \text{(B8)}$$

The resulting nonlinear equation then takes the following form:

$$-\psi_1(-\infty) = \frac{\pi}{\Omega'}e^{-i\omega_0 t}\int_0^\infty d\tau \rho(t-\tau)e^{i\omega_0\tau}$$

$$+ \frac{\pi}{2\omega_0^2\Omega'}e^{-i\omega_0 t}\int_0^\infty d\tau \int_0^\infty d\tau_1 \int_0^{t-\tau} d\tau_4$$

$$\times \int_0^\infty d\tau_3 \frac{\tau+\tau_1}{\tau_3}[1-e^{2i\omega_0\tau_3}]\rho(t-\tau-\tau_1)$$

$$\times [\dot\rho^*(\tau_4-\tau-\tau_1)\rho(\tau_4-\tau_3)$$

$$- \rho^*(\tau_4-\tau-\tau_1)\dot\rho(\tau_4-\tau_3)]. \qquad \text{(B9)}$$

Using the relations $\psi_1(-\infty) \equiv a\exp(-i\omega_0 t)$ and $\rho = L_1 a + L_2\, da/dt$ and making the substitutions Eqs. (39), (40) we obtain the final nonlinear equation (41).

APPENDIX C: NUMERICAL SOLUTION OF EQ. (43)

The governing equation (43) for the real constants R and σ in Eq. (42) is in the form

$$-ie^{i\phi} = R^2 I(\sigma), \qquad \text{(C1)}$$

where $\phi \cong 0.363$, and

$$I(\sigma) \equiv -\int_0^\infty dx \int_0^x dz\, \frac{z\exp\left(i\sigma\ln\left(\frac{(1+x)(1+z)}{1+x+z}\right)\right)}{(1+x)^2(1+z)^2(1+x+z)^2}$$

$$\times \left\{ \frac{2+i\sigma}{2-i\sigma}\frac{z+x}{1+z+x} - \frac{z}{1+x} - \frac{x}{1+z} \right\}$$

$$= \int_0^\infty \left(-\frac{2+i\sigma}{2-i\sigma}f(x) + g(x) \right)$$

$$\times \exp\left(i\sigma\ln\left(\frac{(1+x)^2}{1+2x}\right) \right) dx, \qquad \text{(C2)}$$

where $f(x)$ and $g(x)$ are polynomial ratios combined with a logarithmic function. The argument χ of the function $I(\sigma) = |I(\sigma)|\exp(i\chi(\sigma))$ determines σ implicitly through the relation

$$\chi(\sigma) = \phi - \frac{\pi}{2} + 2\pi k, \quad k = 0, \pm 1, \pm 2, \ldots, \qquad \text{(C3)}$$

and $R = |I(\sigma)|^{-1/2}$. From Eq. (C2) we infer that $\chi(\sigma)$ is an odd function in σ. The argument of $I(\sigma)$ has been calculated numerically[25] based on the single integral, as well as the
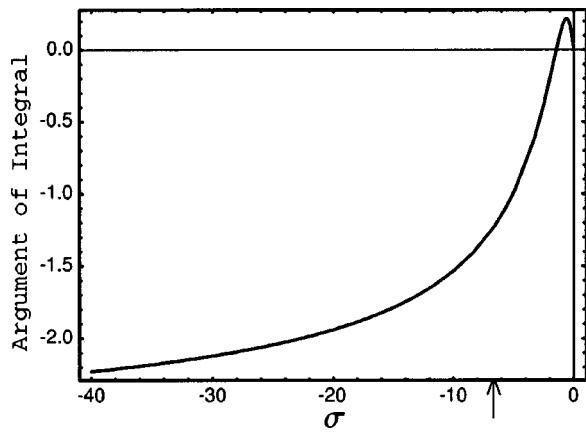
FIG. 8. The argument χ of $I(\sigma)$ as a function of σ based on the numerical solution of single integral formulation in Eq. (C2).

double integral in Eq. (C2), and the results agree. The functional dependence of χ on σ is illustrated in Fig. 8. For $\phi \cong 0.363$ we find a solution of Eq. (C3) for $\sigma = -6.5$, as indicated with the arrow in Fig. 8.

[1] K. McGuire, R. Goldston, M. Bell *et al.*, Phys. Rev. Lett. **50**, 891 (1983).
[2] M. N. Bussac, R. Pellat, D. Edery, and J. L. Soule, Phys. Rev. Lett. **35**, 1638 (1975).
[3] M. N. Rosenbluth, R. Y. Dagazian, and P. H. Rutherford, Phys. Fluids **16**, 1894 (1973).
[4] L. Chen, R. B. White, and M. N. Rosenbluth, Phys. Rev. Lett. **52**, 1122 (1984).
[5] B. Coppi and F. Porcelli, Phys. Rev. Lett. **57**, 2272 (1986).
[6] W. W. Heidbrink and G. Sadler, Nucl. Fusion **34**, 535 (1994).
[7] R. Betti and J. P. Freidberg, Phys. Rev. Lett. **70**, 3428 (1993).
[8] F. Porcelli, R. Stankiewicz, H. L. Berk, and Y. Z. Zhang, Phys. Fluids B **4**, 3017 (1992).
[9] G. Foggacia and F. Romanelli, Phys. Plasmas **2**, 227 (1995).
[10] B. Coppi, S. Migliuolo, and F. Porcelli, Phys. Fluids **31**, 1630 (1988).
[11] B. N. Breizman, H. L. Berk, M. S. Pekker, F. Porcelli, G. V. Stupakov, and K. L. Wong, Phys. Plasmas **4**, 1559 (1997).
[12] B. B. Kadomtsev, *Plasma Turbulence* (Academic, New York, 1965).
[13] B. B. Kadomtsev and O. P. Pogutse, Sov. Phys. JETP **39**, 1012 (1973).
[14] H. R. Strauss, Phys. Fluids **19**, 134 (1976).
[15] A. Ödblom, P. J. Catto, and S. I. Krasheninnikov, Phys. Plasmas **6**, 3239 (1999).
[16] H. L. Berk, B. N. Breizman, and M. S. Pekker, Plasma Phys. Rep. **23**, 778 (1997).
[17] B. N. Breizman, J. Candy, F. Porcelli, and H. L. Berk, Phys. Plasmas **5**, 2326 (1998).
[18] H. L. Berk, B. N. Breizman, and M. Pekker, Phys. Rev. Lett. **76**, 1256 (1996).
[19] A. Ödblom, B. N. Breizman, S. E. Sharapov, T. C. Hender, and V. P. Pastukhov, Proceedings of Contributed Papers, 27th European Physical Society Conference on Contr. Fusion and Plasma Physics, Budapest, 2000, edited by K. Szegö, T. N. Todd, and S. Zoletnik (Europhysics Conference Abstracts, 2000), Vol. 24B, p. 1525.
[20] W. M. Manheimer and C. N. Lashmore-Davies, *MHD and Microstabilities in Confined Plasma*, Adam Hilger series on Plasma Physics (Bristol, UK, 1989).
[21] R. Fitzpatrick and T. C. Hender, Phys. Fluids B **3**, 644 (1991).
[22] R. G. Littlejohn, J. Plasma Phys. **29**, 111 (1983).
[23] H. L. Berk, B. N. Breizman, and H. Ye, Phys. Fluids B **5**, 1506 (1993).
[24] B. N. Breizman and S. E. Sharapov, Plasma Phys. Controlled Fusion **37**, 1057 (1995).
[25] Wolfram Research Inc., MATHEMATICA, Version 3.0 (Wolfram Research Inc., Champaign, IL, 1996).